Journal of Materials Chemistry C

ROYAL SOCIETY OF CHEMISTRY

PAPER

View Article Online
View Journal | View Issue

Cite this: J. Mater. Chem. C, 2022, 10, 18189

Multichannel charge transfer enhanced radiative decay and RISC in TADF materials containing multiple donors and acceptors†

Zhaolong He,[a] Jiuyan Li, *[a] Di Liu, *[ab] Huihui Wan,[c] Yongqiang Mei[a] and Chunlong Shi[a]

Coexistence of through-bond charge transfer (TBCT) and through-space charge transfer (TSCT) is observed to strongly enhance the performance of thermally activated delayed fluorescence (TADF) materials that contain multiple donors and acceptors. A group of TADF emitters were developed with carbazole as the donor, benzophenone as the acceptor, and phenylene as the linking bridge. TBCT was responsible for the TADF feature of the *para*-linked analogue ***p*-tCz-BP**, while both TBCT and TSCT were observed in the *ortho*-linked isomer ***o*-tCz-BP**. The multiple-donor–acceptor analogue **D-tCz-D-BP** was proved to exhibit multi-channel TBCT and TSCT processes with more near-degenerate excited states and more TSCT (81.0%) contribution than ***o*-tCz-BP** (66.3%). Thus **D-tCz-D-BP** combines the merits of both the high oscillator strength of ***p*-tCz-BP** and the tiny energy splitting (ΔE_{ST}) between the lowest singlet and triplet excited states caused by the twisted conformation of ***o*-tCz-BP**, leading to a high rate constant of radiation (k_r) of 1.01×10^7 s^{-1}, of reverse intersystem crossing (k_{risc}) of 0.56×10^6 s^{-1} and a high photoluminescence quantum yield of 96.8%. The sky-blue organic light-emitting diode (OLED) of **D-tCz-D-BP** exhibited an external quantum efficiency (EQE) of 24.9%, much higher than those of ***p*-tCz-BP** (6.3%) and ***o*-tCz-BP** (11.1%). **D-tCz-D-BP** was also capable of hosting an orange-red iridium phosphor to form a two-emitting-component white OLED that realized an EQE of 18.8% and a high CRI of 80.

Received 14th September 2022,
Accepted 17th November 2022

DOI: 10.1039/d2tc03875g

rsc.li/materials-c

Introduction

Recently, thermally activated delayed fluorescence (TADF) materials with high electroluminescent (EL) efficiency and low cost have attracted considerable attention as third-generation organic light-emitting diode (OLED) materials.[1,2] Since the spins of the injected charges are uncorrelated, the ratio of singlet excitons to triplet excitons generated by electronic excitation is 1 : 3.[3,4] For TADF emitters, small energy splitting between the lowest singlet and triplet states (ΔE_{ST}) is indispensable to promote triplet to singlet spin conversion *via* an effective reverse intersystem crossing (RISC) process and full utilization of both singlet and triplet excitons for light emission, finally achieving an internal quantum efficiency (IQE) of 100%.[2,5,6] A typical strategy to minimize the ΔE_{ST} is adopting large steric-hindrance induced twisted intramolecular through-bond charge transfer (TBCT) or through-space charge transfer (TSCT) to separate the highest occupied molecular orbital (HOMO) and the lowest unoccupied molecular orbital (LUMO) on the individual electron donor (D) and acceptor (A) unit, which results in small HOMO–LUMO overlaps.[4,7,8] According to Fermi's golden rule, a small ΔE_{ST} favors facilitation of efficient RISC processes and thus increases the reverse intersystem crossing rate (k_{risc}).[9,10] However, small overlap of the HOMO and LUMO usually generates a small oscillator strength (f), radiative decay rate (k_r) and low photoluminescence quantum yield (PLQY).[11,12] Hence, generating a balance between a small ΔE_{ST} and high k_{risc}, k_r and PLQY is essential for excellent TADF materials.

Recently, researchers have reported the combinational effects of TBCT and TSCT in one single molecule, in which the *ortho*-linkage of the D and A units on the phenylene bridge endows large D–A dihedral angles and cofacial interactions with a small D–A spatial distance, leading to small ΔE_{ST} and

[a] Frontiers Science Center for Smart Materials, College of Chemical Engineering, Dalian University of Technology, 2 Linggong Road, Dalian, 116024, China. E-mail: jiuyanli@dlut.edu.cn, liudi@dlut.edu.cn
[b] State Key Laboratory of Luminescent Materials and Devices, South China University of Technology, Guangzhou, 510640, China
[c] Instrumental Analysis Center, Dalian University of Technology, Dalian, 116024, China

† Electronic supplementary information (ESI) available. CCDC 2174202. For ESI and crystallographic data in CIF or other electronic format see DOI: https://doi.org/10.1039/d2tc03875g

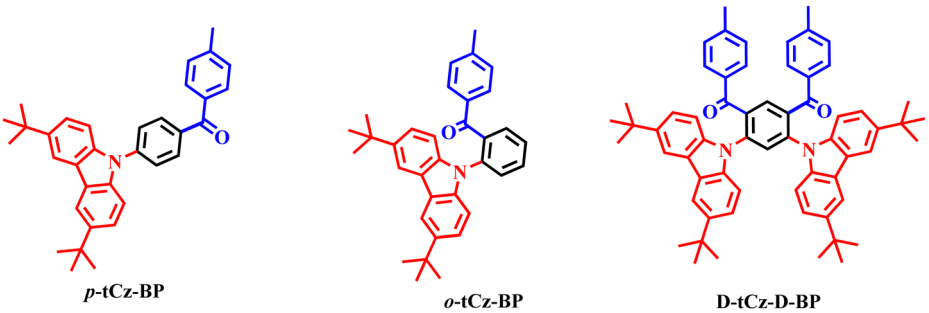

Scheme 1 Chemical structures of ***p*-tCz-BP**, ***o*-tCz-BP** and **D-tCz-D-BP**.

high k_r, k_{risc} and PLQY. For instance, Chi *et al.* adopted a sterically hindered asymmetric D–A–D′ configuration to suppress non-radiative decay and accelerate radiative decay, gaining a high PLQY of 91.9%. As a result, the non-doped emitter (2Cz-DPS) exhibited a high external quantum efficiency (EQE) of 28.7% in OLEDs.[2] Yang *et al.* reported the combinational effect of TBCT and TSCT in one single TADF molecule, which could provide multiple charge transfer pathways, increase the PLQY and reduce the ΔE_{ST} simultaneously, achieving high-efficiency TADF emitters (one of the EQEs had a high value up to 28.1%).[6,13,14] Duan *et al.* developed TADF molecules with *ortho*-linked multiple donor-acceptor (*ortho*-D_n–A) motifs to create near-degenerate excited states for the reinforcement of spin–orbit coupling (SOC). The incorporation of TBCT and TSCT enlarges the oscillator strength (*f*), and the optimal *ortho*-D_3–A compound achieved a high PLQY (100%), k_{risc} (10^6 s^{-1}) and k_r (10^7 s^{-1}) and generated a high EQE over 30% when it acted as the sensitizer for a doped emitter in OLEDs.[15] As mentioned above, the positions or numbers of D and A can affect not only the charge transfer format but also the performance of the emitter.[16–21] Furthermore, some TBCT-TSCT type TADF emitters, especially blue emitting ones, have been used as hosts and/or host emitters to fabricate phosphorescent OLEDs (PhOLEDs) and/or white OLEDs (WOLEDs) at very low doping concentrations.[22,23]

A group of TADF molecules, namely ***p*-tCz-BP**, ***o*-tCz-BP** and **D-tCz-D-BP** (Scheme 1), was designed using tert-butylcarbazole as the donor, benzophenone as the acceptor and phenylene as the linking bridge. The linking style between the donor and acceptor was varied as *para*- or *ortho*- in isomers ***p*-tCz-BP** and ***o*-tCz-BP** to investigate the influence of D–A charge transfer to the electronic and TADF properties. Through-bond charge transfer (TBCT) was observed in the *para*-linked ***p*-tCz-BP**, where significant HOMO–LUMO overlapping results in a large *f* of 0.258 and a high k_r of 2.25×10^7 s^{-1} but a relatively large ΔE_{ST} (0.23 eV). While both TBCT and through-space charge transfer (TSCT) were proved in the *ortho*-linked ***o*-tCz-BP**, which has a more twisted conformation and small spatial distance of *ortho*-substituted donor–acceptor moieties accompanied by a small HOMO–LUMO overlap, resulting in a tiny ΔE_{ST} of near zero and a high k_{risc} of 2.85×10^6 s^{-1}. By increasing the donor and acceptor contents in **D-tCz-D-BP**, *i.e.* with double *ortho*-linked donor–acceptor pairs on the phenylene bridge, multi-channel charge transfer was confirmed including *para*-TBCT, *ortho*-TBCT, and TSCT. **D-tCz-D-BP** shows more near-degenerate excited states and a higher intramolecular TSCT (81.0%) contribution than ***o*-tCz-BP** (66.3%). By inheriting the advantages of both ***p*-tCz-BP** and ***o*-tCz-BP**, **D-tCz-D-BP** exhibits a good balance between large *f* and small ΔE_{ST}, thus achieving a high k_r of 1.01×10^7 s^{-1}, a high k_{risc} of 0.56×10^6 s^{-1} and a high PLQY of 96.8% simultaneously. The sky-blue OLED with **D-tCz-D-BP** as the doped emitter gained a maximum EQE of 24.9%, much higher than those of ***p*-tCz-BP** (6.3%) and ***o*-tCz-BP** (11.1%). **D-tCz-D-BP** also acted as an excellent host or a host emitter for a red iridium (III) complex (Ir2) to fabricate a red phosphorescence OLED and a two-emitting-component white OLED with an acceptable performance.

Results and discussion

Synthesis and characterization

The chemical structures of ***p*-tCz-BP**, ***o*-tCz-BP** and **D-tCz-D-BP** are shown in Scheme 1, and their synthesis is provided in Scheme S1 in the ESI.† The important intermediates 1, 2, and 3, *i.e.* the brominated phenylene intermediates, were first synthesized according to the literature methods.[24–26] Then the nucleophilic addition of these brominated intermediates with 4-methylbenzaldehyde in the presence of *n*-BuLi followed by further oxidation with pyridinium chlorochromate generated the final products ***p*-tCz-BP**, ***o*-tCz-BP** and **D-tCz-D-BP** at moderate yields. These compounds have good solubilities in common organic solvents and could be purified by column chromatography and repeated recrystallization. Details of the syntheses and structure characterization are provided in the ESI.†

Theoretical calculations

Density functional theory (DFT) calculation at the B3LYP-D3BJ/def2-SVP level and time-dependent DFT (TD-DFT) calculation at the PBE0/def2-SVP level were performed to gain insights into the electronic and structural properties of these compounds. As shown in Fig. 1a, in the optimized ground-state geometries of ***p*-tCz-BP**, ***o*-tCz-BP** and **D-tCz-D-BP**, the dihedral angles between the linking phenylene and donor moieties are 51.3°, 68.9° and 62.6°, respectively. Evidently, the carbazole donor ring was

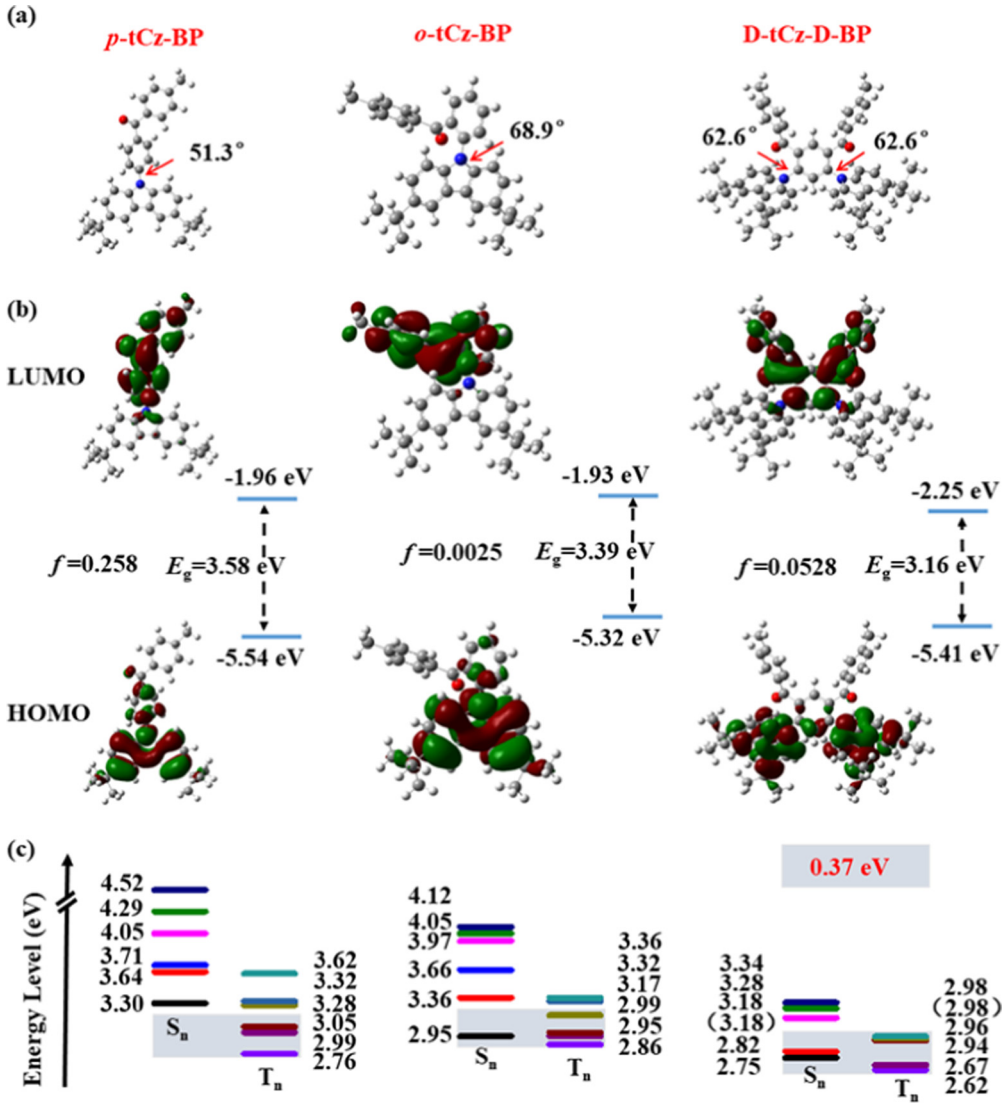

Fig. 1 (a) Optimized ground geometries, (b) HOMO/LUMO distributions, and (c) energy level diagram of the PBE0/def2-SVP calculated excited states of ***p*-tCz-BP**, ***o*-tCz-BP** and **D-tCz-D-BP**.

more twisted due to the steric hindrance effect when the donor and acceptor moieties are *ortho*-linked on the phenylene bridge. Meanwhile, in ***o*-tCz-BP** and **D-tCz-D-BP** molecules, the donor moieties show a tilted face-to-face alignment with the *ortho*-substituted acceptor moieties at a minimum spatial distance of 2.94 Å and 2.96 Å (Fig. 1a) between the non-hydrogen atoms, respectively, suggesting a more effective intramolecular π–π interaction between donor and acceptor and indicating the possible existence of TSCT. In contrast, TBCT seems exclusive in the ***p*-tCz-BP** molecule as the *para*-substitution increases the spatial distance between the donor and acceptor. The oscillator strengths (*f*) of these molecules were calculated to be 0.258, 0.0025 and 0.0528, respectively. It was found that **D-tCz-D-BP** inherits the twisted configuration and small donor–acceptor spatial distance from ***o*-tCz-BP**, but further gains a balance in the *f* values between ***p*-tCz-BP** and ***o*-tCz-BP** and finally reveals a moderate *f* of 0.0528. The frontier molecular orbitals (FMOs) distribution is shown in Fig. 1b, and the HOMOs of these molecules are mainly located on the tCz units while the LUMOs are located on the BP units. Clearly, large orbital overlap on the phenylene bridge is observed for ***p*-tCz-BP**, leading to a large theoretical ΔE_{ST} of 0.54 eV (Fig. 1c). In contrast, small orbital overlaps were observed for ***o*-tCz-BP** and **D-tCz-D-BP**, and thus achieving small theoretical ΔE_{ST}s of 0.09 and 0.13 eV, respectively. The suitable HOMO and LUMO overlap on the phenylene bridge suggests that charge can also be transferred through the phenylene moiety directly, confirming the possibility of TBCT in these molecules. It is interesting that the HOMO and HOMO−1 of **D-tCz-D-BP** are nearly degenerated (Table S1, ESI†), and may both contribute to the CT states. Fig. 1c shows the TD-DFT calculated excited states of these molecules. For **D-tCz-D-BP**, there are many near-degenerate singlet (S_1–S_2) and triplet excited states (T_2–T_6), which are close to the T_1 state with small energy gaps and thus

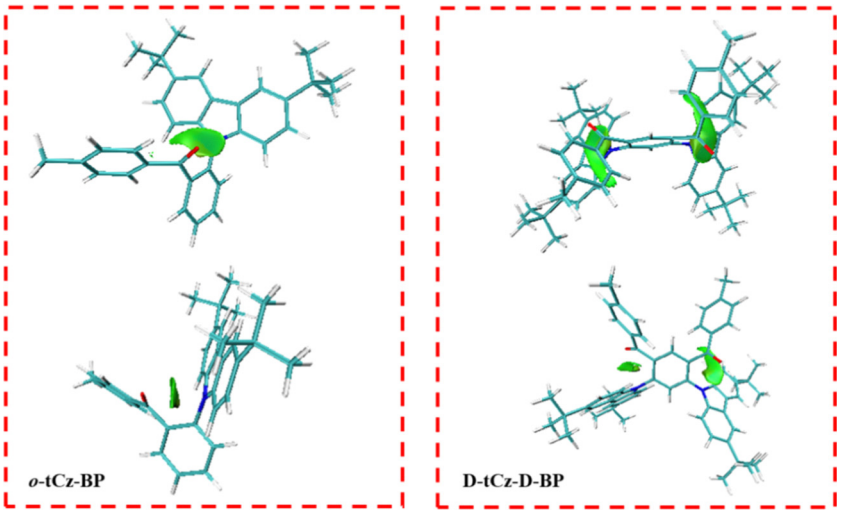

Fig. 2 IGMH isosurface maps of ***o*-tCz-BP** and **D-tCz-D-BP** from different perspectives (isosurfaces of δg^{inter} = 0.004 a.u.).

definitely promote an efficient multichannel RISC process. The spin–orbit coupling matrix elements (SOCME) between these states were also calculated and are illustrated in Table S2 (ESI†). It was reported that within an empirical energy range of 0.37 eV and a high SOC value (>0.3 cm^{-1}),[6,27,28] the numbers of valid RISC channels (blue-grey background) found in ***p*-tCz-BP**, ***o*-tCz-BP** and **D-tCz-D-BP** are 0, 4, and 10, respectively. According to Fermi's golden rule, k_{risc} is proportional to $\langle S|\hat{H}_{soc}|T/\Delta E_{ST}\rangle$, in which $\langle S|\hat{H}_{soc}|T\rangle$ is the spin orbit coupling (SOC) matrix element between the excited singlet (S) and triplet (T) states.[9,10] Hence, ***o*-tCz-BP** and **D-tCz-D-BP** favor possessing a faster RISC pathway. More importantly, **D-tCz-D-BP** possesses much more valid RISC channels along with an increased oscillator strength (f = 0.0528), indicating the multi-donor–acceptor molecular architecture may be favorable for the light-emitting performance theoretically. Of course, the energy of 0.37 eV is within an empirical range that only represents a rough trend. This empirical energy range should be considered along with the experimentally determined energy values when they are used to interpret the RISC and TADF mechanisms.

To explore the existence of weak intramolecular interactions between donor and acceptor, the independent gradient model based on the Hirshfeld partition of molecular density (IGMH) analyses in Multiwfn was studied,[29–31] and the sign $(\lambda_2)\rho$ colored IGMH isosurface maps are shown in Fig. 2. The green regions of the IGMH isosurface maps show the presence of obvious intramolecular interactions, indicating that intramolecular through-space charge transfer can occur between donor and acceptor fragments in ***o*-tCz-BP** and **D-tCz-D-BP**. By integrating the transition density that was localized on/not on the phenylene linker, the proportions of TBCT/TSCT contribution to the S_1 states were calculated to be 33.7%/66.3% and 19.0%/81.0% for ***o*-tCz-BP** and **D-tCz-D-BP**, respectively. The natural transition orbital (NTO) and triplet state spin density distribution (TSDD) were calculated to analyze the transition characteristics (Fig. S1, ESI†). Apparently, three molecules reveal a typical charge-transfer (CT) feature in their S_1 states; ***p*-tCz-BP** shows a combined local-excited triplet state (^{3}LE) and charge-transfer triplet states (^{3}CT), while ***o*-tCz-BP** and **D-tCz-D-BP** exhibit a strong ^{3}CT feature instead of the ^{3}LE feature. Accordingly, different linking styles of donor and acceptor and multiple donor–acceptor pairs in one single molecule will generate different TBCT/TSCT proportions and subtly determine the excited states.[19,21]

According to the optimized ground state geometries of these molecules, TD-DFT calculations were conducted to reveal the excited state energy-levels of the corresponding fragment molecules (Fig. S2, ESI† and Fig. 1c). The characters of low-lying singlet and triplet states other than S_1 and T_1 were also obtained by analyzing the hole and particle distributions in NTO analyses (Fig. S1, ESI†). Combined with fragment molecular calculations and NTO analyses of these molecules, it was found that the ^3LE_A and ^3LE_D were located energetically close to the ^{3}CT (TBCT and TSCT) states or mixed with the ^{3}CT states. According to the El-Sayed rule, spin–orbital coupling between the ^{1}CT and ^{3}CT states is forbidden due to identical spatial orbital angular momentums, while that between the ^{1}CT and ^{3}LE states is permitted.[32,33] Meanwhile, if ^{1}CT and ^{3}CT states stem from different charge transfer excited states, *e.g.* TBCT and TSCT, the SOC between ^{1}CT and ^{3}CT states should also be allowed. The ^3LE_A, ^3LE_D and mixed ^{3}LE and ^{3}CT states can therefore serve as intermediate excited states between the ^{3}CT and ^{1}CT states to mediate spin–orbital coupling and promote the RISC process.[17,33,34] According to Fermi's golden rule, k_{risc} is proportional to $\langle S|\hat{H}_{soc}|T\rangle/\Delta E_{ST}$. Hence, both large SOC and small ΔE_{ST} are optimum for a faster RISC process.

Based on the excited state alignment and the calculated SOC, the corresponding charge transfer channels and RISC mechanisms are proposed for these three emitters in Fig. 3. ***p*-tCz-BP** is characterized by an exclusive *para*-TBCT pathway and a relatively large ΔE_{ST}, which are not favorable for an efficient RISC process. However, due to the existence of intermediate excited states and considerable SOC between S_1 and T_3 states with different spatial orbital angular momentums, the T_1

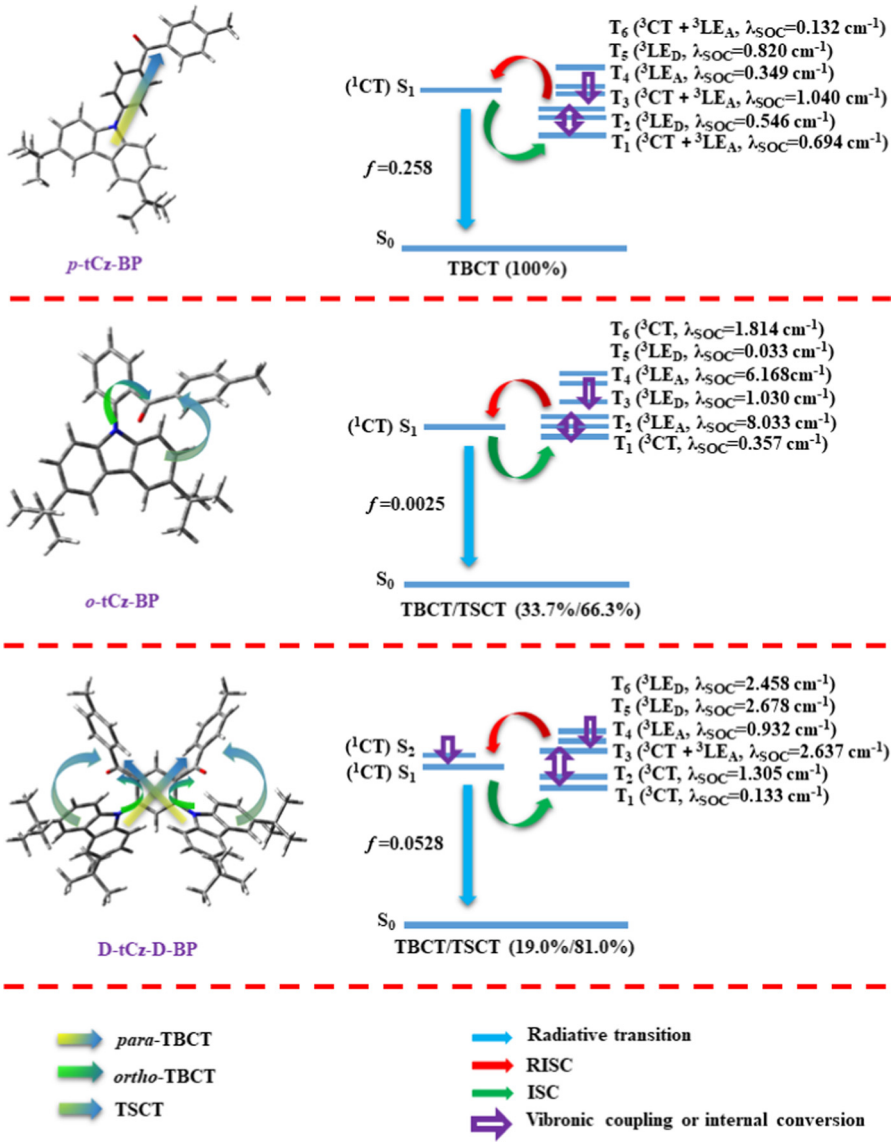

Fig. 3 Charge transfer models (left) and the excited state alignment and supposed RISC mechanism (right) for ***p*-tCz-BP**, ***o*-tCz-BP**, and **D-tCz-D-BP**.

state can still be pumped to T_2 and T_3 states *via* vibrational coupling (VC) and thus transformed into the S_1 state *via* RISC. Additionally, a large ΔE_{ST} and oscillator strength (f) normally refer to inferior k_{risc} and superior k_r, respectively. As for ***o*-tCz-BP** that has an *ortho*-linked and face-to-face donor and acceptor, there are two intramolecular charge transfer channels, *i.e.* *ortho*-TBCT (33.7%) and TSCT (66.3%), which lead to an extremely small ΔE_{ST}. At the same time, due to small energy differences between these triplet excited states, T_1 (^{3}CT) and T_6 (^{3}CT) states can be transformed into the intermediate excited states of T_2 (^3LE_A), T_3 (^3LE_D) and T_4 (^3LE_A) *via* vibrational coupling (VC) and internal conversion (IC), and then converted to S_2 (^{1}CT) or S_1 (^{1}CT) states. Based on the small energy gaps between these intermediate triplet excited states and S_1 state and large SOC values, a multichannel RISC process is reasonable for ***o*-tCz-BP** and rather high k_{risc} values can be expected. With increasing the contents of both donor and acceptor to form **D-tCz-D-BP**, the rich position relationships between the donor and acceptor generated three different types of charge transfer pathways, including *para*-TBCT, *ortho*-TBCT and TSCT. As calculated in Fig. 2, the content ratios are TBCT (19%, *para*-TBCT + *ortho*-TBCT) and TSCT (81%). Within an empirical energy range of 0.37 eV, there are much more intermediate triplet excited states that can be transformed into S_1 or S_2 states, most of which have a high SOC value (>0.3 cm^{-1}), predicting the feasibility of a multichannel RISC process. Based on high SOC values, small ΔE_{ST} and considerable oscillator strength (f), superior k_{risc} and k_r can be safely anticipated simultaneously for **D-tCz-D-BP.**

Crystal structure and electrochemical properties

X-ray single crystal diffraction analysis for **D-tCz-D-BP** was performed. The details for the single crystal are listed in Table S3 in the ESI.† As shown in Fig. 4a, the dihedral angles between donors and the phenylene bridge are 61.95° and

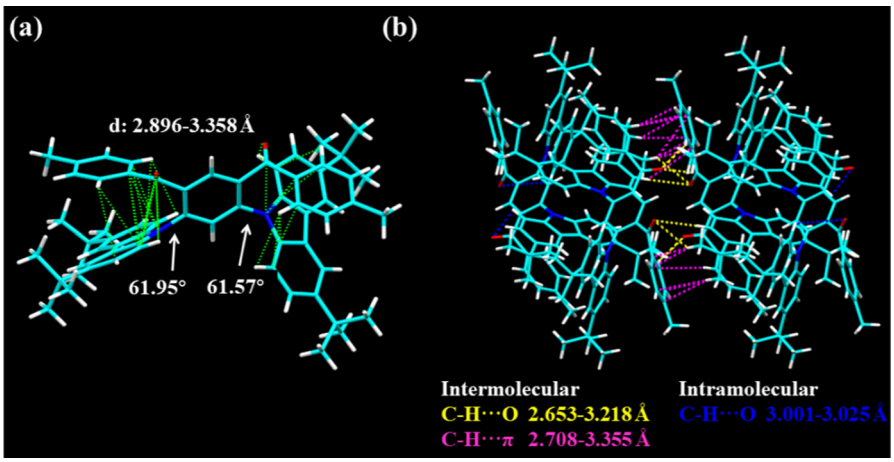

Fig. 4 Single crystal structure (a) and packing diagram (b) of **D-tCz-D-BP**.

61.57°, and the minimum π–π spatial distance between the non-hydrogen atoms in the acceptor and donor planes is 2.910 Å, confirming the coexistence of *ortho*-TBCT and TSCT effects. These results are in agreement with the theoretical calculations. It can be observed that there are multiple intermolecular and intramolecular interactions in its crystal packing (Fig. 4b), which are expected to restrict intramolecular motions and enhance the molecular rigidify, thus alleviating non-radiative decay and improving emission efficiency.

The electrochemical properties of these compounds were examined by cyclic voltammetry (CV) in DCM (anodic scan) and DMF solutions (cathodic scan), as shown in Fig. S3 (ESI†). Using the onset potentials of the first oxidation and reduction wave (E_{ox}^{onset} and E_{red}^{onset}), the HOMO and LUMO energies for all these compounds were estimated according to the empirical equations $E_{HOMO} = -e(E_{ox}^{onset} + 4.4)$ and $E_{HOMO} = -e(E_{red}^{onset} + 4.4)$. The HOMO and LUMO levels were −5.55/−2.79, −5.52/−2.67 and −5.58/2.89 eV for ***p*-tCz-BP**, ***o*-tCz-BP** and **D-tCz-D-BP**, respectively. The different LUMOs for regioisomers ***p*-tCz-BP** and ***o*-tCz-BP** might be ascribed to different substitution positions, which finally impact the acceptor strength.[18] The electrochemical data are listed in Table S4 (ESI†).

Photophysical properties

The ultraviolet-visible (UV-vis) absorption in dilute toluene (10^{-5} M) and photoluminescence (PL) spectra in different solvents at room temperature (RT) of ***p*-tCz-BP**, ***o*-tCz-BP** and **D-tCz-D-BP** are shown in Fig. 5a and the relevant photophysical data are summarized in Table S4 (ESI†). The high-energy absorption bands in the range of 290–350 nm should be assigned to local transitions of tCz and BP fragments, and the corresponding weak and broad bands above 355 nm are attributed to intramolecular charge transfer (ICT) from the donor to the acceptor. The PL spectra of ***p*-tCz-BP** and ***o*-tCz-BP** in solvents with different polarities exhibit broad and structureless bands, which could be assigned to the typical ICT emission, and the bathochromic shift displays a distinct positive solvatochromism, confirming their PL all originate from the CT excited states. The PL spectra of **D-tCz-D-BP** exhibit a dual emission feature in low polar solvents like hexane or toluene, in which the short-wavelength and long-wavelength bands should be assigned to the LE state and CT state emission, respectively, since the LE state emission at around 450 nm is almost independent of the solvent polarity in position but

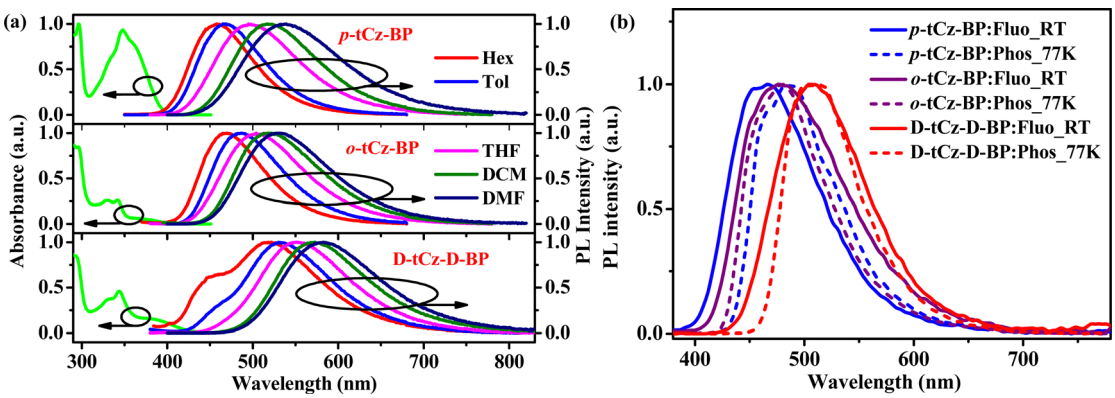

Fig. 5 UV-vis absorption and PL spectra in different solvents at RT (a) and fluorescence spectra in PPF films at room temperature and phosphorescence spectra (with a 60 ms delay time following pulsed excitation) of the same films at 77 K (b) for ***p*-tCz-BP**, ***o*-tCz-BP** and **D-tCz-D-BP**.

Table 1 Photophysical data of the investigated molecules in 8 wt% doped PPF films at room temperature

Compound	ΔE_{ST} [eV]	Φ [%]	Φ_{PF}/Φ_{DF} [%]	Φ_p/Φ_d [%]	τ_{PF} [ns]	τ_{DF} [μs]	k_r/k_{nr} [10^6 s^{-1}]	k_{isc} [10^6 s^{-1}]	k_{risc} [10^6 s^{-1}]
***p*-tCz-BP**	0.23	28.8	6.7/22.1	23.2/76.8	3.0	528.8	22.5/55.7	259.1	0.0082
***o*-tCz-BP**	0.08	57.8	1.3/56.5	2.2/97.8	5.5	15.9	2.33/1.70	177.9	2.85
D-tCz-D-BP	0.15	96.8	12.1/84.7	12.5/87.5	12.0	14.4	10.1/0.33	73.2	0.56

gradually gave place to the CT emission band with increasing solvent polarity while the CT emission band exhibited a distinct positive solvatochromism.

According to the onsets of fluorescence spectra at room temperature and phosphorescence spectra at 77 K measured in 8 wt% doped PPF films (Fig. 5b), the S_1 and T_1 energies of ***p*-tCz-BP**, ***o*-tCz-BP** and **D-tCz-D-BP** were experimentally determined to be 3.10/2.87, 3.00/2.92 and 2.86/27.1 eV, and the corresponding ΔE_{ST} were calculated to be 0.23, 0.08 and 0.15 eV, respectively (Table 1). The experimental ΔE_{ST} values of ***o*-tCz-BP** and **D-tCz-D-BP** were in good agreement with the TD-DFT calculated values. The S_1 energy level of ***o*-tCz-BP** was smaller than that of ***p*-tCz-BP**, which could be ascribed to the enhanced charge transfer (two charge transfer channels) in the ***o*-tCz-BP** molecule. The smaller ΔE_{ST} (0.08 eV) of ***o*-tCz-BP** could also be ascribed to the enhanced charge transfer (especially TSCT) and greatly reduced S_1 energy due to reduced HOMO–LUMO overlaps caused by the twisted structure. For a similar reason, both greatly reduced S_1 and T_1 energy levels were observed for **D-tCz-D-BP** owing to the multi-donor–acceptor interactions,[19] resulting in small ΔE_{ST} values of 0.15 eV. The relevant photophysical data are summarized in Table 1 and Table S4 (ESI†).

To confirm the TADF properties, the transient PL decay of these emitters doped in PPF (2,8-bis(diphenylphosphoryl)dibenzo[b,d]furan) film was measured at RT (Fig. 6 inset). Each transient curve consists of a prompt fluorescence (PF) and the delayed emission components. The emission at different delay times was detected with spectra identical to the PF (Fig. S6, ESI†), suggesting that the delayed emission and the PF originated from the same singlet excited state, *i.e.* the delayed fluorescence (DF). The PF have lifetimes (τ_{PF}) of 3.0, 5.5, and 12.0 ns (Fig. S7, ESI†), and the DF with lifetimes (τ_{DF}) of 528.8, 15.9 and 14.0 μs for ***p*-tCz-BP**, ***o*-tCz-BP** and **D-tCz-D-BP** were obtained, and the corresponding absolute PLQYs (Φ) were measured as 28.8%, 57.8% and 96.8%, respectively. The long DF lifetime and low PLQY of ***p*-tCz-BP** can be ascribed to large ΔE_{ST}. Although the τ_{DF} of ***o*-tCz-BP** and **D-tCz-D-BP** are almost equally short, the much higher PLQY of **D-tCz-D-BP** definitely favors

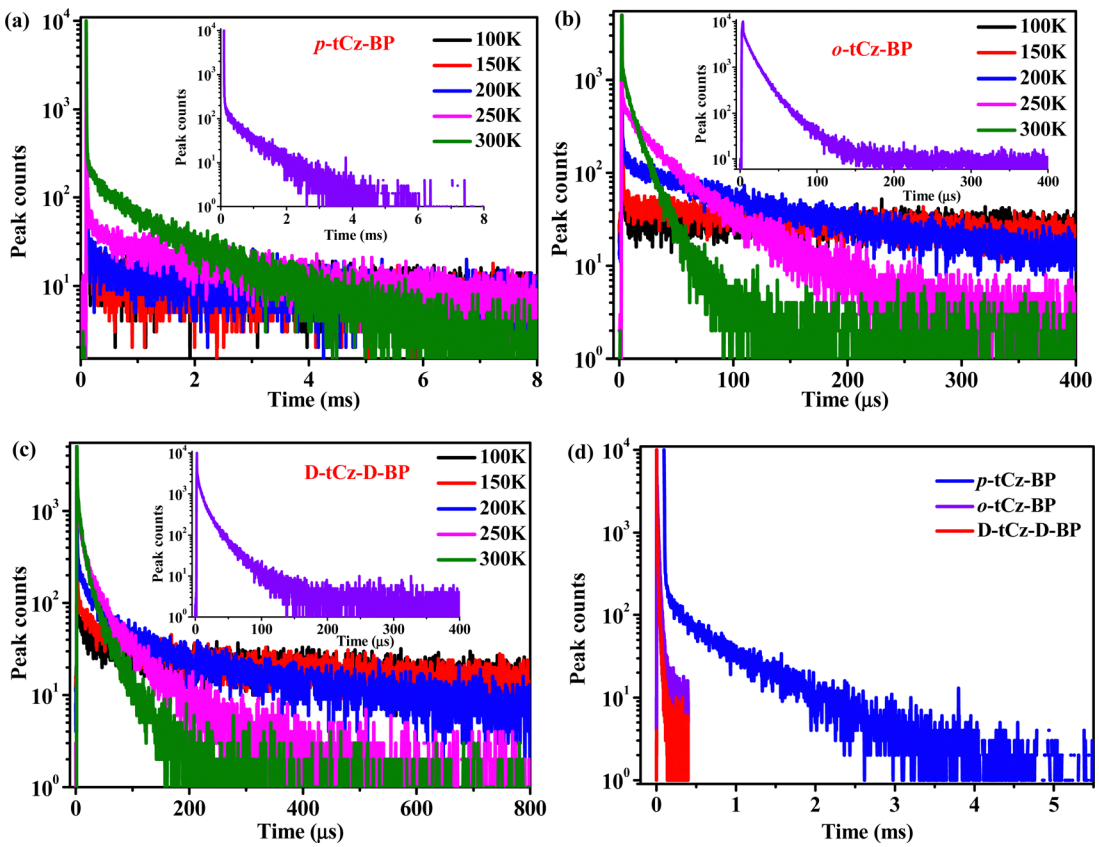

Fig. 6 Temperature-dependent PL decay curves of (a) ***p*-tCz-BP**, (b) ***o*-tCz-BP** and (c) **D-tCz-D-BP** in the doped PPF films (8 wt%), and time-resolved transient PL decay curves at room temperature (insets of a, b, and c) and their comparison (d).

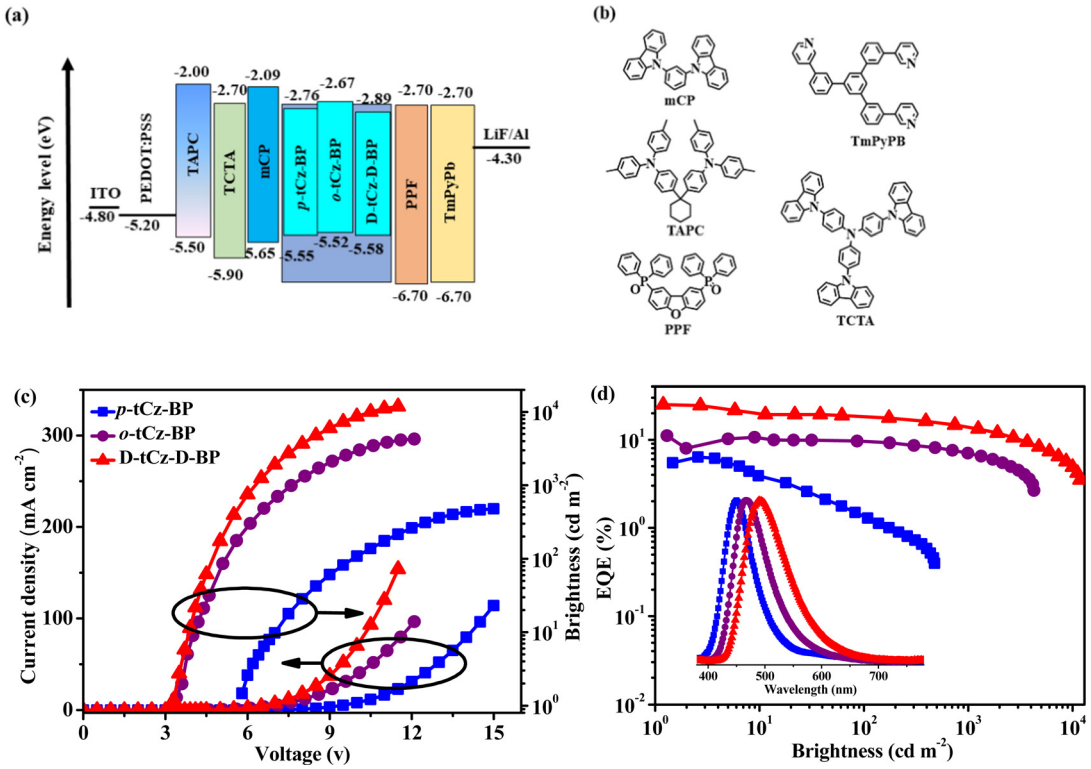

Fig. 7 (a) Device configuration and energy level diagrams, (b) chemical structures of the materials used in the OLEDs, (c) *J*–*V*–*B* characteristics, and (d) EQE curves and EL spectra (inset) of the single color OLEDs.

gaining a good TADF performance. The positive temperature dependence of the delayed emission intensity (Fig. 6) along with the small ΔE_{ST} values confirmed the TADF nature for these three emitters.[35] Taking into account the contributions of the prompt (Φ_p) and delayed (Φ_d) components to the total PLQYs (Φ), the Φ_{DF} gradually increases from 22.1%, *via* 56.5% to 84.7% for ***p*-tCz-BP**, ***o*-tCz-BP** and **D-tCz-D-BP**, respectively, happening to be consistent with the trend of the TSCT proportions contributed to the S_1 state (0, 66.3% and 81.0%, sequentially). According to the transient PL data and PLQY values, all relevant rate constants of different kinetic processes were calculated following the reported equations.[36,37] The rate constants of radiation (k_r) were calculated to be 2.25×10^7 s^{-1}, 0.23×10^7 s^{-1} and 1.01×10^7 s^{-1}, the rate constants of RISC (k_{risc}) were calculated to be 0.0082×10^6 s^{-1}, 2.85×10^6 s^{-1} and 0.56×10^6 s^{-1}, and the rate constants of non-radiation (k_{nr}) were calculated to be 55.7×10^6 s^{-1}, 1.70×10^6 s^{-1} and 0.33×10^6 s^{-1} for ***p*-tCz-BP**, ***o*-tCz-BP** and **D-tCz-D-BP**, respectively. The high k_r of ***p*-tCz-BP** and **D-tCz-D-BP** should be ascribed to large *f* values, the high k_{risc} of ***o*-tCz-BP** and **D-tCz-D-BP** should be attributed to small ΔE_{ST}, favorable SOC, and much more valid RISC channels. Due to the restricted intramolecular motions and enhanced molecular rigidity in the crystal packing, **D-tCz-D-BP** gained the lowest k_{nr}, favoring alleviation of the non-radiative decay and improving the emission efficiency. Obviously, **D-tCz-D-BP** with multi-donor–acceptor *para*/*ortho*-linked architecture not only possesses a high PLQY, low k_{nr} and high rate of TSCT contribution, but it also combines the merits of ***p*-tCz-BP** and ***o*-tCz-BP**. The photophysical data of the investigated molecules are listed in Table 1.

Electroluminescent devices

To further investigate the electroluminescence (EL) performances of ***p*-tCz-BP**, ***o*-tCz-BP** and **D-tCz-D-BP**, multilayer OLEDs were fabricated with the device configuration of indium tin oxide (ITO)/poly-(3,4ethylenedioxythiophene):poly(styrene

Table 2 EL data summary of the blue to sky-blue (A, B, C), red (R) and white (W) OLEDs

Device	V_{on}[a] [V]	η_c[b] [cd A^{-1}]	η_p[b] [lm W^{-1}]	η_{ext}[b] [%]	λ_{EL}[c] [nm]	FWHM[d] [nm]	CIE(x,y)[e]
A	5.8	6.7/1.4/0.4	3.5/0.5/0.1	6.3/1.4/0.4	450	62	0.16,0.12
B	3.4	18.5/16.0/13.5	17.0/9.8/6.3	11.1/9.6/8.2	468	74	0.17,0.23
C	3.3	54.8/40.3/34.6	52.2/28.2/19.7	24.9/18.5/15.7	490	90	0.22,0.40
R	3.5	26.3/25.2/22.8	20.2/12.8/9.4	21.0/20.2/18.3	618	69	0.62,0.36
W	3.2	39.6/29.3/26.2	38.8/21.1/15.2	18.8/13.5/12.1	500,606	—	0.41,0.42

[a] V_{on}, turn-on voltage at 1 cd m^{-2}. [b] η_c, η_p, η_{ext}: the current efficiency, power efficiency, and external quantum efficiency for devices A, B, C, R and W, and the values are in the order of maximum/at 100 cd m^{-2}/at 500 cd m^{-2}. [c] λ_{EL}, EL peak wavelength at 8 V. [d] FWHM, full width at half maximum. [e] CIE(x,y), Commission International de I'Eclairage coordinates at 8 V.

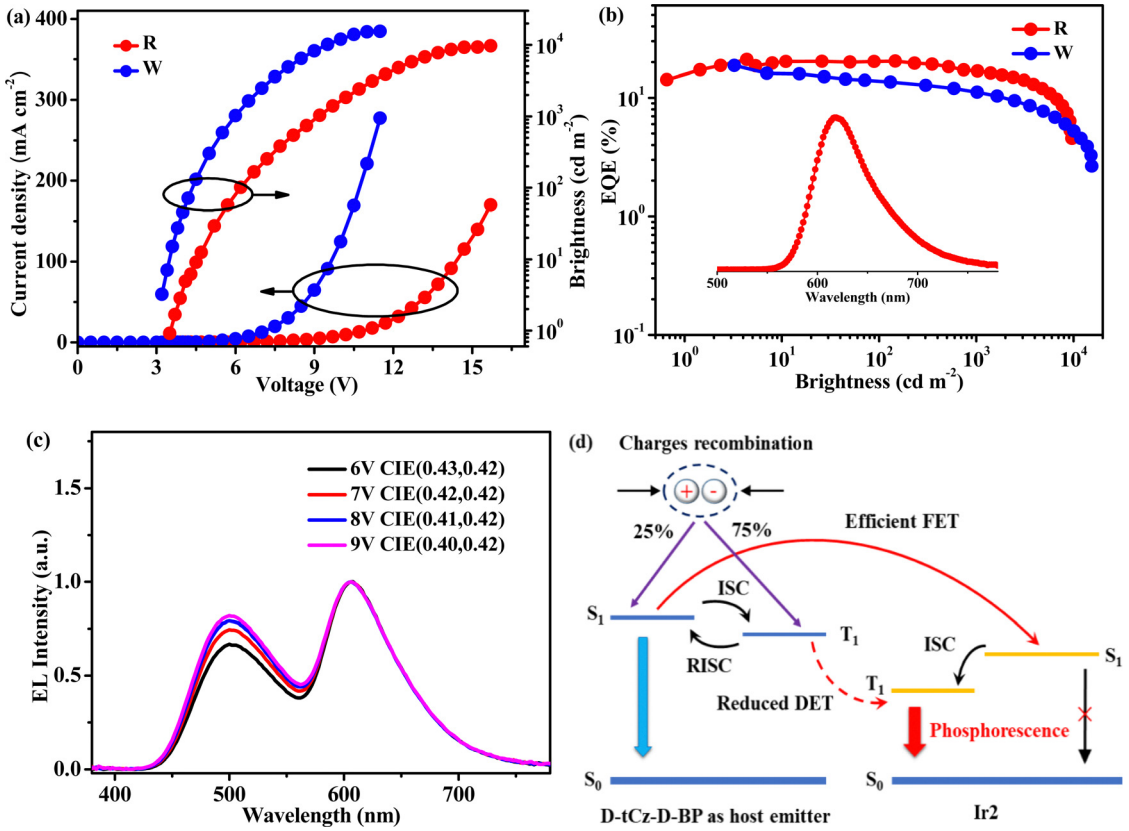

Fig. 8 (a) *J–V–B* characteristics, (b) EQE curves (inset: EL spectra of device R), (c) EL spectra of the white device W, and (d) proposed mechanism of the white device W (Abbreviations: FET: Förster energy transfer, DET: Dexter energy transfer).

sulfonic acid) (PEDOT:PSS, 40 nm)/1,1-bis[(di-4tolylamino)-phenyl]cyclohexane (TAPC, 20 nm)/4,4′,4″-tri(Ncarbazolyl) triphenylamine (TCTA, 5nm)/(1,5-bis(9-carbazolyl)benzene) (mCP, 5 nm)/PPF:dopant (8 wt%, 20 nm)/(2,8-bis(diphenylphosphoryl)-dibenzo[b,d]furan) (PPF, 5 nm)/(3,3′-(5′-(3-(pyridine-3-yl)phenyl)-[1,1′:3′,1″-terphenyl]-3,3″-diyl)dipyridine (TmPyPB, 40 nm)/LiF (1 nm)/Al (200 nm). The energy level diagram of the OLEDs and the chemical structures of these materials are depicted in Fig. 7a and b. In these devices, PEDOT:PSS and TAPC served as the hole-injection layer (HIL) and the hole-transporting layer (HTL), PPF as the host material, TCTA, mCP and PPF as exciton-blocking materials, and TmPyPB and LiF as the electron-transporting layer (ETL) and electron-injection layer (EIL), respectively. The EL characteristics of devices A, B and C based on ***p*-tCz-BP**, ***o*-tCz-BP** and **D-tCz-D-BP** were depicted in Fig. 7c and d and the corresponding device performances were summarized in Table 2. As shown in Fig. 7c and d, emission peaks at 450, 466, and 490 nm for ***p*-tCz-BP**, ***o*-tCz-BP** and **D-tCz-D-BP** were obtained, respectively, corresponding to CIE coordinates of (0.16, 0.11), (0.17, 0.23) and (0.22, 0.40). Spectral bathochromic shifts should be ascribed to the progressively enhanced intramolecular charge transfer (ICT) strength. According to the EL spectra and current density–voltage–brightness (*J–V–B*) characteristics, the maximum current efficiency (CE), maximum power efficiency (PE) and EQE were calculated to be 6.7 cd A^{-1}, 3.5 lm W^{-1} and 6.3% for device A, 18.5 cd A^{-1}, 17.0 lm W^{-1} and 11.1% for device B and 54.8 cd A^{-1}, 52.2 lm W^{-1} and 24.9% for device C, respectively. The inferior EL performances of device A could be ascribed to the lower PLQY, larger ΔE_{ST}, large k_{nr} and longer τ_{DF} of ***p*-tCz-BP**, and the inferior EL performances of device B could be ascribed to the small *f*, moderate PLQY and relatively large k_{nr} of ***o*-tCz-BP**. On the contrary, the superior EL performance of device C should be ascribed to the absolutely high PLQY, large k_r and k_{risc}, and small ΔE_{ST} and k_{nr} of **D-tCz-D-BP**. Evidently, thanks to the multichannel charge transfer feature gained in **D-tCz-D-BP**, both the radiation transition and RISC were efficiently enhanced and balanced with an extremely high PLQY (96.8%), high k_{risc} (0.56×10^6 s^{-1}) and low k_{nr} (0.33×10^6 s^{-1}), which finally resulted in the excellent performance of the **D-tCz-D-BP**-based TADF-OLED.

Inspired by the excellent performance of **D-tCz-D-BP** in its TADF-OLEDs, it was also explored **D-tCz-D-BP**as a host to sensitize iridium phosphors to fabricate phosphorescence OLEDs with a configuration of ITO/PEDOT:PSS (40 nm)/TAPC (20 nm)/mCP (5 nm)/**D-tCz-D-BP**:Ir2 (3 wt%, 20 nm)/PPF (5 nm)/TmPyPB (40 nm)/LiF (1 nm)/Al (200nm) (device R). The home-made Ir2 was used as the red emitting dopant and its structure is shown in Fig. S8 in the ESI.†[38] Fig. 8a–c illustrate the *J–V–B* characteristics, efficiency curves and the EL spectra of device R, and the related EL data are summarized in Table 2. At an optimized doping concentration of 3 wt%, device R displayed red emission with a peak at 618 nm and CIE coordinates of (0.62, 0.36). The single emission from the phosphorescent dopant indicated the sufficient energy transfer from the host

to dopant. The device R displayed a maximum CE of 26.3 cd A^{-1} and EQE of 21.0%. The pure red emission from the iridium dopant with the acceptable efficiency of device R manifests that **D-tCz-D-BP** is a promising host material for a phosphorescent emitter. With further reducing the doping concentration of Ir2 in **D-tCz-D-BP** to 0.2 wt% (device W, Fig. 8a–c), both the sky-blue emission from the **D-tCz-D-BP** host and the red phosphorescence from the Ir2 dopant were obtained simultaneously, generating warm white emission (Fig. 8c). Device W exhibited a maximum η_c of 39.6 cd A^{-1}, η_p of 38.8 lm W^{-1}, and η_{ext} of 18.8%. With the driving voltage going from 6 to 9 V, the CIE coordinates showed a slight change from (0.43,0.42) to (0.40, 0.42), and a CRI from 79 to 80, respectively. The good performance of the WOLED including acceptable efficiency and the high CRI value should be ascribed to the intrinsically excellent TADF feature and good charge transporting ability of **D-tCz-D-BP** when it acted as the host emitter in a white OLED. As shown in Fig. 8d, at such a low doping concentration of 0.2 wt%, the Förster energy transfer from the singlet excitons of **D-tCz-D-BP** to the iridium dopant molecules followed by the easy and efficient intersystem crossing of the iridium phosphor should dominate the excitation of phosphorescent dopant molecules.

Conclusions

By grafting two pairs of *ortho*-linked carbazole donor-benzophenone acceptors on the phenylene bridge, a novel TADF emitter **D-tCz-D-BP** was developed. Multichannel charge transfer, including *para*-TBCT (through-bond charge transfer), *ortho*-TBCT and TSCT (through-space charge transfer), was proved by single crystal analysis and theoretical calculations in **D-tCz-D-BP**, which essentially enhanced both the radiation and RISC processes and thus resulted in a high k_r of 1.01×10^7 s^{-1}, a high PLQY of 96.8%, and a high k_{risc} of 0.56×10^6 s^{-1}. The sky-blue TADF-OLED with **D-tCz-D-BP** as the doped emitter exhibited a maximum EQE of 24.9%, much higher than those of the reference analogues ***p*-tCz-BP** (6.3%) and ***o*-tCz-BP** (11.1%) that contain either a *para*- or *ortho*-linked donor–acceptor. **D-tCz-D-BP** also exhibited good performance with a high EQE of 18.8% and a high CRI of 80 in the two-emitting-component white OLED when it acted as the host emitter for a red iridium phosphor. It was demonstrated that multichannel charge transfer is a practical strategy to design high-performance TADF emitters for OLED applications.

Author contributions

Zhaolong He: conceptualization, investigation, writing – original draft. Jiuyan Li: funding acquisition, investigation, supervision, writing – review and editing. Di Liu: investigation, project administration, resource, supervision. Huihui Wan: spectra acquisition and structure characterization. Yongqiang Mei: data curation, visualization. Chunlong Shi: formula analysis, software.

Conflicts of interest

There are no conflicts of interest to declare.

Acknowledgements

We thank the National Natural Science Foundation of China (U1801258 and 22078051), the Fundamental Research Funds for the Central Universities (DUT22LAB610) and the Open Fund of the State Key Laboratory of Luminescent Materials and Devices (South China University of Technology, 2021-skllmd-03) for financial support of this work.

References

1 X. Q. Wang, S. Y. Yang, Q. S. Tian, C. Zhong, Y. K. Qu, Y. J. Yu, Z. Q. Jiang and L. S. Liao, *Angew. Chem., Int. Ed.*, 2021, **60**, 5213–5219.
2 Z. Yang, Z. Mao, C. Xu, X. Chen, J. Zhao, Z. Yang, Y. Zhang, W. Wu, S. Jiao, Y. Liu, M. P. Aldred and Z. Chi, *Chem. Sci.*, 2019, **10**, 8129–8134.
3 P. K. Samanta, D. Kim, V. Coropceanu and J. L. Bredas, *J. Am. Chem. Soc.*, 2017, **139**, 4042–4051.
4 X. Li, J. Li, D. Liu, D. Li and R. Dong, *New J. Chem.*, 2020, **44**, 9743–9753.
5 H.-Z. Li, F.-M. Xie, K. Zhang, Y. Shen, W. Zhou, Y.-Q. Li, W.-J. Wang and J.-X. Tang, *Chem. Eng. J.*, 2022, **436**, 135234.
6 X. Zheng, R. Huang, C. Zhong, G. Xie, W. Ning, M. Huang, F. Ni, F. B. Dias and C. Yang, *Adv. Sci.*, 2020, **7**, 1902087.
7 X. Liang, Z. L. Tu and Y. X. Zheng, *Chem. – Eur. J.*, 2019, **25**, 5623–5642.
8 Z. G. Wu, H. B. Han, Z. P. Yan, X. F. Luo, Y. Wang, Y. X. Zheng, J. L. Zuo and Y. Pan, *Adv. Mater.*, 2019, **31**, 1900524.
9 Z. Lin, R. Kabe, K. Wang and C. Adachi, *Nat. Commun.*, 2020, **11**, 191.
10 J. U. Kim, I. S. Park, C. Y. Chan, M. Tanaka, Y. Tsuchiya, H. Nakanotani and C. Adachi, *Nat. Commun.*, 2020, **11**, 1765.
11 J. Xue, Q. Liang, R. Wang, J. Hou, W. Li, Q. Peng, Z. Shuai and J. Qiao, *Adv. Mater.*, 2019, **31**, 1808242.
12 W. Li, X. Cai, B. Li, L. Gan, Y. He, K. Liu, D. Chen, Y. C. Wu and S. J. Su, *Angew. Chem., Int. Ed.*, 2019, **58**, 582–586.
13 X. Lv, Y. Wang, N. Li, X. Cao, G. Xie, H. Huang, C. Zhong, L. Wang and C. Yang, *Chem. Eng. J.*, 2020, **402**, 126173.
14 M. Ouyang, L. Xing, Q. Chen, H. Huang, M. Zhu, K. Hu, Y. Liu, W.-C. Chen, Y. Huo and C. Yang, *J. Mater. Chem. C*, 2021, **9**, 1678–1684.
15 T. Huang, Q. Wang, S. Xiao, D. Zhang, Y. Zhang, C. Yin, D. Yang, D. Ma, Z. Wang and L. Duan, *Angew. Chem., Int. Ed.*, 2021, **60**, 23771–23776.
16 D. Zhang, X. Song, A. J. Gillett, B. H. Drummond, S. T. E. Jones, G. Li, H. He, M. Cai, D. Credgington and L. Duan, *Adv. Mater.*, 2020, **32**, 1908355.
17 H. Noda, X. K. Chen, H. Nakanotani, T. Hosokai, M. Miyajima, N. Notsuka, Y. Kashima, J. L. Bredas and C. Adachi, *Nat. Mater.*, 2019, **18**, 1084–1090.

18 N. A. Kukhta, H. F. Higginbotham, T. Matulaitis, A. Danos, A. N. Bismillah, N. Haase, M. K. Etherington, D. S. Yufit, P. R. McGonigal, J. V. Gražulevičius and A. P. Monkman, *J. Mater. Chem. C*, 2019, **7**, 9184–9194.
19 A. Danos, D. Gudeika, N. A. Kukhta, R. Lygaitis, M. Colella, H. F. Higginbotham, A. N. Bismillah, P. R. McGonigal, J. V. Grazulevicius and A. P. Monkman, *J. Mater. Chem. C*, 2022, **10**, 4737–4747.
20 G. Haykir, M. Aydemir, A. Danos, S. Gumus, G. Hizal, A. P. Monkman and F. Turksoy, *Dyes Pigm.*, 2021, **194**, 109579.
21 F.-M. Xie, J.-X. Zhou, Y.-Q. Li and J.-X. Tang, *J. Mater. Chem. C*, 2020, **8**, 9476–9494.
22 J. Zeng, J. Guo, H. Liu, Z. Zhao and B. Z. Tang, *Adv. Funct. Mater.*, 2020, **30**, 2000019.
23 H. Chen, H. Liu, P. Shen, J. Zeng, R. Jiang, Y. Fu, Z. Zhao and B. Z. Tang, *Adv. Opt. Mater.*, 2021, **9**, 2002019.
24 T. Sudyoadsuk, S. Petdee, P. Chasing, P. Therdkatanyuphong, C. Kaiyasuan, W. Waengdongbung, S. Namuangruk and V. Promarak, *Dyes Pigm.*, 2021, **195**, 109721.
25 Y. H. Lee, S. Park, J. Oh, S.-J. Woo, A. Kumar, J.-J. Kim, J. Jung, S. Yoo and M. H. Lee, *Adv. Opt. Mater.*, 2018, **6**, 1800385.
26 H. L. Lee, W. J. Chung and J. Y. Lee, *Small*, 2020, **16**, 1907569.
27 R. Chen, Y. Tang, Y. Wan, T. Chen, C. Zheng, Y. Qi, Y. Cheng and W. Huang, *Sci. Rep.*, 2017, **7**, 6225.
28 Y. Tao, R. Chen, H. Li, J. Yuan, Y. Wan, H. Jiang, C. Chen, Y. Si, C. Zheng, B. Yang, G. Xing and W. Huang, *Adv. Mater.*, 2018, **30**, 1803856.
29 T. Lu and F. Chen, *J. Comput. Chem.*, 2012, **33**, 580–592.
30 C. Lefebvre, G. Rubez, H. Khartabil, J. C. Boisson, J. Contreras-Garcia and E. Henon, *Phys. Chem. Chem. Phys.*, 2017, **19**, 17928–17936.
31 T. Lu and Q. Chen, *J. Comput. Chem.*, 2022, **43**, 539–555.
32 M. A. El-Sayed, *J. Chem. Phys.*, 1963, **38**, 2834–2838.
33 Y. Song, M. Tian, R. Yu and L. He, *ACS Appl. Mater. Interfaces*, 2021, **13**, 60269–60278.
34 M. K. Etherington, J. Gibson, H. F. Higginbotham, T. J. Penfold and A. P. Monkman, *Nat. Commun.*, 2016, **7**, 13680.
35 L. Gan, Z. Xu, Z. Wang, B. Li, W. Li, X. Cai, K. Liu, Q. Liang and S. J. Su, *Adv. Funct. Mater.*, 2019, **29**, 1808088.
36 W. Li, B. Li, X. Cai, L. Gan, Z. Xu, W. Li, K. Liu, D. Chen and S. J. Su, *Angew. Chem., Int. Ed.*, 2019, **58**, 11301–11305.
37 R. Dong, J. Li, D. Liu, D. Li, Y. Mei, M. Ma and J. Jiang, *Adv. Opt. Mater.*, 2021, **9**, 2100970.
38 H. Tian, D. Liu, J. Li, M. Ma, Y. Lan, W. Wei, R. Niu and K. Song, *New J. Chem.*, 2021, **45**, 11253–11260.